ACTA IMEKO
ISSN: 2221-870X
March 2019, Volume 8, Number 1, 56 - 63

Dual-channel electrodermal activity and an ECG wearable sensor for measuring mental stress from the hands

Antonio Affanni[1]

[1] *Polytechnic Department of Engineering and Architecture, University of Udine, via delle Scienze 206, 33100 Udine, Italy*

ABSTRACT
The paper describes the design and characterisation of a dual-channel electrodermal activity (EDA) and ECG sensor for acquiring data from the hands. The need for dual-channel data acquisition is due to the removal of motion artefacts that may happen when EDA is measured on subjects when they are moving their hands in their everyday activities. The ECG channel is measured from the hands using the same electrodes that have already been used for EDA. This choice reduces the invasiveness of ECG measurement with respect to the usual vests or chest bands. The characterisation demonstrates high-level performance of the sensor in terms of linearity and jitter, even if the measurement on the hands provides a weaker ECG signal with respect to chest derivations. Even when the subject is using their hands, no artefacts were found in extracting the heart rate from ECG.

Section: RESEARCH PAPER

Keywords: electrodermal activity; stress measurement; ECG sensors

Citation: Antonio Affanni, Dual-channel electrodermal activity and an ECG wearable sensor for measuring mental stress from the hands, Acta IMEKO, vol. 8, no. 1, article 9, March 2019, identifier: IMEKO-ACTA-08 (2019)-01-09

Section Editor: Sergio Rapuano, University of Sannio, Italy

Received March 06, 2018; **In final form** October 23, 2018; **Published** March 2019

Corresponding author: Antonio Affanni, e-mail: antonio.affanni@uniud.it

1. INTRODUCTION

In the recent past, studies focusing on stress or distress among healthy people in several conditions (e.g. in the workplace, while driving, playing videogames) have exponentially increased. Several bio-signals are measured while the subjects of such studies are doing tasks e.g. photoplethysmogram (PPG) [1], electroencephalogram (EEG) [2], electromyogram (EMG) [3], electrocardiogram (ECG) [4], [5], electrodermal activity (EDA) [6]-[10], and many others.

The present paper presents the design and characterisation of a sensor for stress recognition, focusing on drivers, using two EDA channels and an ECG channel acquiring data from the hands. The need for two channels for EDA measurement is derived from the fact that usually the motion of the hands (from where EDA is mainly acquired) provides a huge motion artefact, which makes the acquired data unreliable if hand motions are not tracked [8]; for this reason, in most scientific literature, the subjects are sitting, with still hands. However, when doing several everyday tasks (e.g. driving a car), people need two hands, and this is a problem in the acquisition of EDA. For this reason, in the present paper, we present our development of a dual-channel EDA sensor with the aim of using both channels to discriminate the motion artefact from sympathetic activity.

In order to evaluate heart rate (HR) and its variability (HRV), in scientific literature, subjects usually need to wear a chest strap or a vest, which makes the measurement setup uncomfortable for the subject, especially if the measurement is acquired in real life (e.g. driving) instead of a laboratory for scientific experiments. In this work, different to previous works [5]-[8], we have two goals: The first is to acquire the ECG trace from the hands using the same electrodes used for EDA; and the second is to process two EDA signals in order to increase the robustness of the data with respect to motion artefacts. In the recent past, we presented a study [5] in which EDA and ECG were acquired simultaneously using traditional electrodes disposition on the chest by means of a special t-shirt; however, dressing in a special t-shirt with wet electrodes is not very comfortable for the user. On the other hand, in [8], we demonstrated that the motion artefact during driving is as high as the EDA signal or higher; thus, some correction to the acquired data must be applied. Adding a second channel to the EDA, we are able to discriminate EDA peaks in a more robust way (e.g. using independent component analysis or other algorithms) than previous works.

The measurement of EDA reads a signal controlled by the sympathetic nervous system. EDA measurement methodologies can be exosomatic (skin conductance response [SCR] or galvanic skin response [GSR]) or endosomatic (namely skin potential

response [SPR]). The first method measures the conductance of the skin, which changes when the subject is stimulated by external events; this happens because the sympathetic nervous system activates the sweating glands in order to sweat. The second method directly measures the nervous pulse, which activates the sweat glands. This second method provides more complex signals than the first, but its readout is faster since it directly acquires the nervous pulse from the sympathetic nervous system [11]; moreover, it is less prone to electrode impedance changes due to temperature or sweating of the hands.

The SPR measurement measures the differential voltage on the skin between a place where there is a high density of sweat glands (mainly the palms of the hands) and a place where sweat glands are fewer (mainly the backs of the hands). In recent literature [12]-[14], several papers have measured ECG and EDA simultaneously (also with commercial solutions). However, ECG is acquired on the chest, and EDA is measured by means of SCR, which cannot provide a fast readout of the signal.

The study of ECG and the consequent HRV has been a matter of study of hundreds of scientific papers. Heart activity is mainly controlled by the sympathetic nervous system and partially by the parasympathetic nervous system (vagus nerve). These two signals control HRV with different aims and speeds of intervention. The sympathetic nervous system slowly varies, while the parasympathetic nervous system varies quickly.

The post-process of HRV is still an open issue in the literature (frequency domain, time domain or other methods are discussed), especially in short-term measurements, where there is a need to know beat-to-beat information [15]-[19]. EDA is a good estimator of short-term sympathetic activity, and simultaneous measurement of ECG and EDA can improve knowledge of HRV, especially in short-term data acquisition.

In this scenario, it is important to have a wearable, wireless, and comfortable instrument that is able to measure both the ECG and EDA without the need for wearing many electrodes on the body.

The paper is organised as follows: Section 2 provides a description of the system. Section 3 provides the metrological characterisation of the sensor and shows the efficacy of the simultaneous measurement of ECG and dual-channel SPR with moving hands. Finally, conclusions are drawn.

2. SENSOR DESCRIPTION

The wearable EDA + ECG system is shown in Figure 1(a). Three disposable Ag/AgCl electrodes are placed on each hand: on the palm, on the back, and on the wrist. The wrist electrodes provide a reference potential VREF, and the bio-signals are acquired as differential voltages present on the skin. In particular, three analogue front-end blocks, shown in Figure 1(b), acquire the difference between the palm and the back of the right hand (SPR1 signal); the difference between the palm and the back of the left hand (SPR2 signal); and the difference between the back of the left hand and the back of the right hand (ECG signal). Each conditioning analogue front end has the architecture shown in Figure 1(c).

The conditioned analogue signals are acquired by means of the A/D on board a DSP, which sends data via WiFi to a laptop (tablet or smartphone).

The system is operated by a single 3.7 V 2000 mAh lithium polymer battery and is rechargeable by means of a USB plug. Since current consumption of the sensor in transmission mode is 200 mA, the system can transmit data for 10 hours of continuous acquisition, by far longer than typical EDA sessions, which are in the order of one hour.

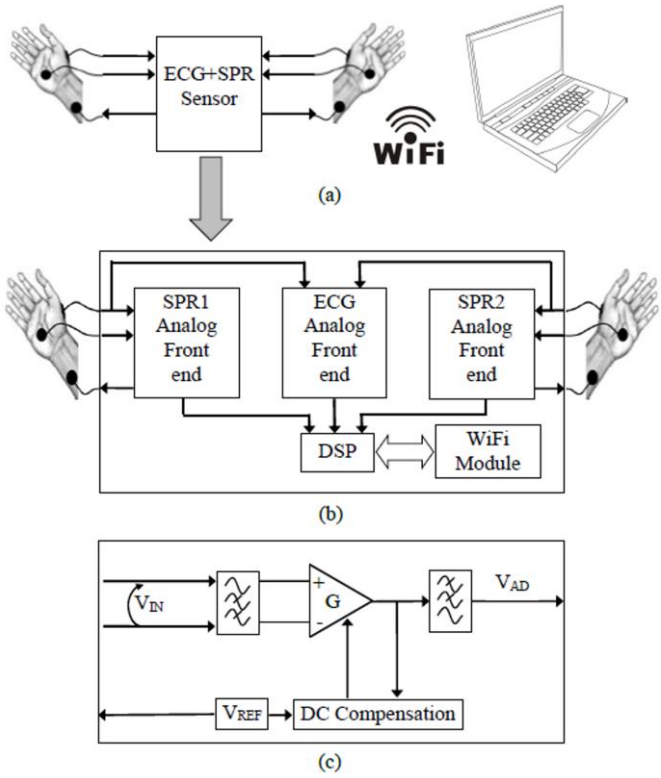

Figure 1. (a) Overall system block diagram; (b) Sensor block diagram; (c) Analogue front-end block diagram.

2.1. Analogue front end description

Referring to Figure 1(c), each analogue front end acquires a low-level differential voltage V_{IN} (either SPR_1, SPR_2, or ECG) and, by proper signal conditioning, provides voltage V_{AD}, which can be acquired by the A/D converter on the DSP.

The V_{IN} voltage is firstly filtered with passive first-order high-pass filters, whose input impedance is 100 MΩ, by far higher than skin output impedance (in the order of 100 kΩ), thus reducing the load uncertainty to less than 1 %. The cut-off frequency of the input filter is $(2\pi\tau_L)^{-1}$=0.05 Hz. Then, an instrumentation amplifier with gain G (throughout the paper, G_{SPR} and G_{ECG} are used for the SPR and ECG signals, respectively) amplifies the differential signal, and at its output, there is a third order, Sallen-Key, anti-alias filter with time constant τ_H ($\tau_{H,SPR}$ and $\tau_{H,ECG}$ for the SPR and ECG signals, respectively). The DC compensation block acts as a time integrator (with time constant τ_I) of the difference between the amplifier output and V_{REF}. The feedback loop composed of the amplifier and the DC compensation block acts as a high-pass filter with cut-off frequency $(2\pi\tau_I)^{-1}$, the chosen coincident with $(2\pi\tau_L)^{-1}$=0.05 Hz. In this way, all the DC non-idealities of the amplifier (offset voltage, bias current, offset current) are removed by the DC compensation block [10].

The overall transfer function of the analogue front end thus, in the Laplace domain, results in

$$V_{AD}(s) = V_{REF}(s) + \frac{\tau_L^2 s^2 G}{(1+\tau_L s)^2(1+\tau_H s)^3} V_{IN}(s). \quad (1)$$

The analogue front end is supplied with 3.3 V, and V_{REF} = 1.65 V, at half-supply range.

The gain of the $SPR_{1,2}$ channels is $G_{SPR} \approx 160$, since the input voltage that has a maximum amplitude of ±10 mV must be converted into 3.3 V_{PP}. The bandwidth of the SPR channels results in the range [0.08, 40] Hz with slopes +40 dB/dec for the lower cut off (0.08 Hz) and –60 dB/dec for the higher cut off (40 Hz).

The gain of the ECG channel has been designed as $G_{ECG} \approx 680$, since the input voltage that has a maximum amplitude of ±2.5 mV must be converted into 3.3 V_{PP}. It is noticeable that ECG acquisition on the chest can provide signals with an amplitude of up to ±5 mV, but the measurement on the hands (despite the comfort of using less electrodes) provides a weaker signal; thus the gain of the analogue front end is the quadruple with respect to traditional ECG chest bands. The bandwidth of the ECG channel results in the range [0.08, 160] Hz with slopes +40 dB/dec for the lower cut off (0.08 Hz) and –60 dB/dec for the higher cut off (160 Hz).

2.2. DSP and A/D conversion

ECG and SPR, once filtered and amplified, are sent to the analogue input port of a Digital Signal Processor (DSP), which acquires V_{AD} and sends the acquired data to the WiFi module via a Universal Asynchronous Receiver Transmitter (UART). The DSP, a DSPIC 30F3013 from Microchip, has an on-board 12-bit analogue-to-digital converter and operates at 8 MIPS. The sample rate has been set at 500 Sa/s, which is high enough to capture ECG signals without overloading the CPU and the graphic card of a medium/low-performance tablet when used in real-time mode. The A/D conversion time has been set at 100 µs with the aim of reducing the sampling transient effects far lower than 1 LSB.

2.3. WiFi module

The WiFi module is the USR-WIFI232 from USR IOT, which can operate both as an access point and as a station. In this application, it is configured as an access point so that several laptops or tablets can acquire data at the same time without the need for a server. The baud rate of the data transfer has been set at 115.2 kbps in order to allow for data transmission without crowding the channel.

2.4. Software description

The control panel used to acquire the data is shown in Figure 2. It has been developed in the .NET framework due to the ease of programming the graphical user interfaces (GUIs). The software is designed to communicate with the SPR+ECG sensor and to plot, in real time, the signal showing the graphical markers with their comments when the subject receives some stimuli. At the top left of the GUI, it is possible to connect to the sensor by inserting the IP address of the access point and network SSID, and to start and stop the acquisition. In the middle left of the screen, it is possible to manually insert markers with their description and save the recorded data or load saved data. The top graph shows the left SPR, the middle graph shows ECG, and the bottom graph shows the right SPR.

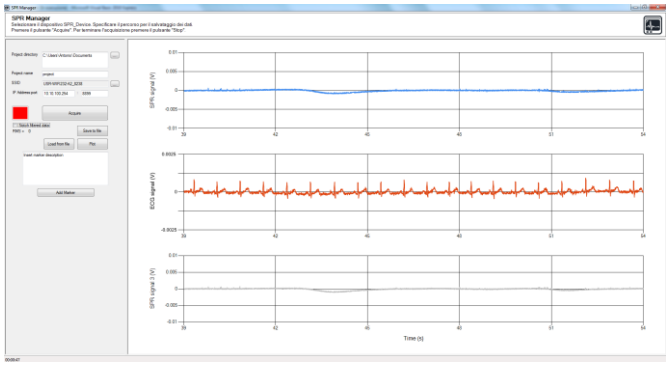

Figure 2. Control panel for the data acquisition.

3. SENSOR CHARACTERISATION AND EXPERIMENTAL RESULTS

Characterisation was done using three different test setups. The first test setup aimed to characterise the analogue and digital circuitry in terms of linearity and bandwidth, sending sinusoidal signals at inputs and measuring the sensor response with the oscilloscope. The second test setup sends, at the input of the sensor, a synthesised ECG generated by a waveform generator. It evaluates the R-R interval of the output with respect to the input using commercial software for ECG and HRV analysis. The aim of this second test setup was to quantify the accuracy of the HR readout by means of the jitter introduced by the sensor. The third test setup showed the necessity of measuring SPR with two channels when hands are moving and shows, for example, the extraction of the HR from ECG acquired from the hands.

3.1. Metrological characterisation

In this subsection, we present the experimental characterisation of the sensor in terms of linearity and bandwidth. For the characterisation, an automatic test benchmark has been developed, connecting an oscilloscope through the LAN and the sensor by means of WiFi. An ad hoc program developed in the Matlab environment controls the built-in waveform generator of the oscilloscope, measures the output of the measurements from the oscilloscope, and a robot code controls saving of the data transmitted from the sensor (by WiFi) to the panel described in Section 2.4. The aim is to automatise all the measurements in order to acquire the largest possible amount of data. After the data collection, the performance was evaluated in accordance with the Guide to the Expression of Uncertainty in Measurement (GUM).

3.1.1. Linearity

The waveform generator built-in digital oscilloscope (RIGOL DS2302A) has been set to provide a sinusoidal voltage V_G with amplitude variable from 0 to 3.3 V_{PP} in 100 linearly spaced steps. The frequency f_0 of the sinusoid is fixed at the centre of the bandwidth, i.e. $f_0 = \sqrt{f_L f_H}$, with value 2 Hz for SPR and 4 Hz for ECG. At the output of the generator, a resistive (0.1 % tolerance of the resistors) attenuator A with output impedance 1 MΩ (to simulate skin behaviour) is connected to each channel of the sensor.

In the case of SPR, $A = 5.568 \cdot 10^{-3}$ ($8 \cdot 10^{-6}$), and in the case of ECG, $A = 1.497 \cdot 10^{-3}$ ($3 \cdot 10^{-6}$).

The uncertainty on the vector $\boldsymbol{V_{IN}}$ (throughout the paper, vectors will be expressed in bold type) thus results in

$$u(\boldsymbol{V_{IN}}) = \sqrt{[A \cdot u(\boldsymbol{V_G})]^2 + [\boldsymbol{V_G} \cdot u(A)]^2}. \quad (2)$$

The RMS value of the output of the analogue front-end V_{AD} is automatically measured with the same oscilloscope over 10 periods of the sinusoid per each input amplitude. The gain is estimated by the least-squares method, supposing that the best estimation of $\boldsymbol{V_{AD}}$ is

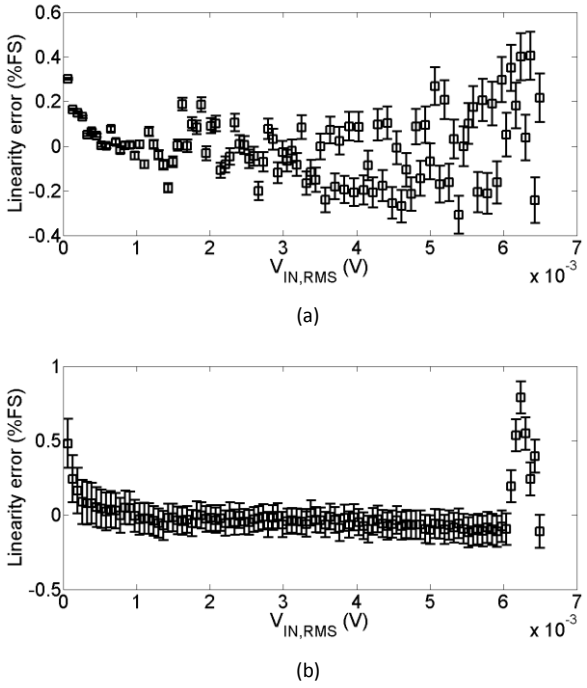

Figure 3. Linearity error of the SPR channels (a) for the analogue front end and (b) for the overall acquisition system. Error bars represent uncertainty in the data.

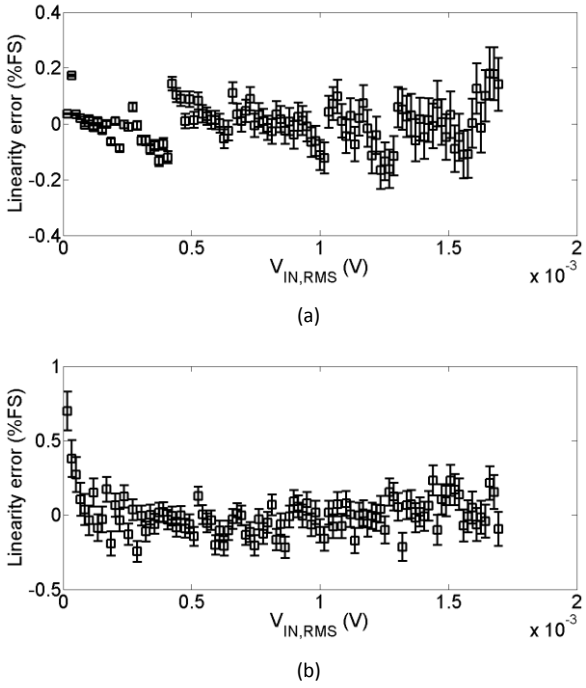

Figure 4. Linearity error of the ECG channel (a) for the analogue front end and (b) for the overall acquisition system. Error bars represent the uncertainty on the data.

$$\widehat{\boldsymbol{V_{AD}}} = G\boldsymbol{V_{IN}} + b\,. \tag{3}$$

Using $\langle\cdot\rangle$ to identify the mean value, the gain G is estimated accordingly as

$$G = \frac{\langle \boldsymbol{V_{IN}}\boldsymbol{V_{AD}}\rangle - \langle \boldsymbol{V_{IN}}\rangle\langle \boldsymbol{V_{AD}}\rangle}{\langle \boldsymbol{V_{IN}}^2\rangle - \langle \boldsymbol{V_{IN}}\rangle^2}. \tag{4}$$

Since both $\boldsymbol{V_{IN}}$ and $\boldsymbol{V_{AD}}$ are affected by uncertainty (from the manual of the oscilloscope $u(\boldsymbol{V_{AD}}) = 0.02 \cdot \boldsymbol{V_{AD}}$ [20]), the uncertainty on the gain is obtained by propagating (4) as

$$u(G) = \sqrt{\sum\left(\frac{\partial G}{\partial V_{IN,i}}u(V_{IN,i})\right)^2 + \sum\left(\frac{\partial G}{\partial V_{AD,i}}u(V_{AD,i})\right)^2}\,, \tag{5}$$

where subscript i means the *i-th* value of the vector corresponding to the *i-th* input amplitude.

After having characterised the gain, the linearity error is estimated as (referring to Equation (3))

$$\boldsymbol{E} = \boldsymbol{V_{AD}} - \widehat{\boldsymbol{V_{AD}}} = \boldsymbol{V_{AD}} - G\boldsymbol{V_{IN}} - b\,. \tag{6}$$

The uncertainty on the linearity error $\boldsymbol{E}$ can be obtained by propagating in Equation (6) the uncertainties in Equation (2) and Equation (5). Since the quantities $\boldsymbol{V_{IN}}$ and $\boldsymbol{V_{AD}}$ are the input and output of an amplifier, respectively, their correlation is expected to be very close to one (in the measured data, it results in 0.999986). Therefore, according to the propagation of uncertainty, the uncertainty estimation of the linearity error E results

$$u(\boldsymbol{E}) = \sqrt{[u(\boldsymbol{V_{AD}}) - G\cdot u(\boldsymbol{V_{IN}})]^2 + [\boldsymbol{V_{IN}}\cdot u(G)]^2 + [u(b)]^2}\,. \tag{7}$$

Regarding the SPR channels, using Equation (2) to Equation (7) results in $G_{SPR} = 145.4 \pm 0.5$, and the linearity error is in the order of 0.5 % FS, corresponding to 50 μV on $\boldsymbol{V_{IN}}$. Figure 3(a) shows the linearity behaviour of the analogue front end. The error bars represent the uncertainty in Equation (7), where the most significant contribution is due to the uncertainty on the oscilloscope $u(\boldsymbol{V_{AD}})$.

Regarding the ECG channel, using Equation (2) to Equation (7) results in $G_{ECG} = 679 \pm 3$ and the linearity error is in the order of 0.2 % FS, corresponding to 5 μV on $\boldsymbol{V_{IN}}$.

Figure 4(a) shows the linearity behaviour of the analogue front end; the error bars represent the uncertainty in Equation (7). Again, the most significant contribution is due to the uncertainty on the oscilloscope $u(\boldsymbol{V_{AD}})$. Referring to Figure 3(a) and Figure 4(a), there is a common trend in linearity between the channels SPR and ECG, which is related to the linearity behaviour of the oscilloscope used for the characterisation.

Using a similar procedure, we characterised the linearity of the overall system, considering the uncertainty introduced by the A/D converter. We acquired the sent data with the control panel and evaluated the RMS value of the data sent over a time interval of 10 periods. Naming N_Q the quantized values of $\boldsymbol{V_{AD}}$ acquired during the characterisation and V_{FS} the full scale of the A/D (i.e. 3.3 V), the estimation of N_Q, according to the least-squares method (3), is

$$\widehat{N_Q} = \frac{2^{12}(G\boldsymbol{V_{IN}} + b)}{V_{FS}} \equiv \alpha\cdot(G\boldsymbol{V_{IN}} + b)\,. \tag{8}$$

Considering from the DSP datasheet that the uncertainty introduced by the A/D is $u_Q = 2$ LSB (which takes into account the quantisation and INL), we have

$$u(N_Q) = \sqrt{\left(\frac{\partial \boldsymbol{N_Q}}{\partial G}u(G)\right)^2 + \left(\frac{\partial \boldsymbol{N_Q}}{\partial \boldsymbol{V_{IN}}}u(\boldsymbol{V_{IN}})\right)^2 + u_Q^2}\,. \tag{9}$$

Similar to Equation (6), we calculate the linearity error of the quantized values E_Q as

$$\boldsymbol{E_Q = N_Q - \widehat{N_Q} = N_Q - \alpha G V_{IN} - \alpha b} \quad (10)$$

and the uncertainty on E_Q as

$$u(\boldsymbol{E_Q}) = \sqrt{\left[u(\boldsymbol{N_Q}) - \alpha G \cdot u(\boldsymbol{V_{IN}})\right]^2 + [\alpha \boldsymbol{V_{IN}} \cdot u(G)]^2 + [\alpha u(b)]^2}\,. \quad (11)$$

Regarding the SPR channels, using Equation (8) to Equation (11), the linearity error is in the order of 0.7 % FS, corresponding to 70 μV on V_{IN}. Figure 3(b) shows the linearity behaviour of the quantised values. The error bars represent the uncertainty in Equation (11). Linearity and its uncertainty are in the same order as those estimated for the analogue front end.

Regarding the ECG channel, using Equation (8) to Equation (11), the linearity error is in the order of 0.7 % FS, corresponding to 18 μV on $\boldsymbol{V_{IN}}$. Figure 4(b) shows the linearity behaviour of the quantised values; and the error bars represent the uncertainty in Equation (11).

3.1.2. Bandwidth

For bandwidth characterisation, the waveform generator has been set to generate a sinusoid with an amplitude of 3.3 V_{PP} and a frequency varying from 0.1 Hz up to 1 kHz, with 10 points per decade, logarithmically spaced. The attenuator described in the previous subsection is placed at the output of the generator. The frequency response of the gain is obtained by evaluating the RMS value of the output over 10 periods with respect to the RMS value of the input. Again, the oscilloscope acquires the RMS value of $\boldsymbol{V_{AD}}$, and the developed control panel acquires the RMS value of the transmitted data.

Figure 6 shows the bandwidth behaviour of the SPR channels. The solid line represents the analogue front end, and the square markers represent the data sent to the laptop. The horizontal line represents the -3 dB amplitude, which defines the bandwidth. The upper cut-off frequency is 40 Hz, and the lower cut-off frequency is lower than 0.1 Hz, which is the limit of the waveform generator (according to the design, it is 0.08 Hz).

Figure 5 shows the bandwidth of the ECG channel, the solid line represents the analogue front end, and the markers represent the entire system. The bandwidth results in the range [0.08, 160] Hz.

3.2. Characterisation with synthesised ECG

For the HRV analysis, accurate recognition of the R-peaks is crucial. For this reason, one of the main problems related to HRV analysis is the jitter introduced by the sensor analogue bandwidth and the sample rate. In this subsection, we show the results of an RR-tachogram acquired by the proposed sensor when the input is a synthesised ECG provided by an arbitrary waveform generator. For the purposes of comparison, the data is simultaneously acquired and saved by an oscilloscope from the sensor and from the generator, used as references. The synthesised ECG has a frequency of 1 Hz and an amplitude of 2 V_{PP}. The input voltage (after the attenuator) thus results in 3 mV_{PP}, and the analogue front-end output is 2 V_{PP}.

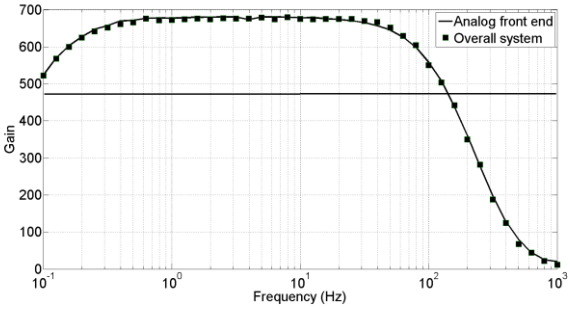

Figure 5. Bode plot of the gain relative to the ECG channel. Continuous line: analogue front end. Markers: overall acquisition system. The horizontal line represents the -3 dB cut off.

Figure 7 shows, as an example, a comparison between the PQRST wave acquired by the oscilloscope from the generator and from $\boldsymbol{V_{AD}}$. The R-peak is shifted because of the analogue bandwidth of the sensor.

In order to quantify the jitter introduced by the sensor, the signal was acquired for 2 mins, and the data of the generator and sensor were processed using Kubios software [21].

Figure 8 shows a comparison between the RR-tachogram acquired by the oscilloscope from the sensor and from the generator. With the same input, the jitter on the R-peak recognition from the proposed sensor is slightly higher than the reference generator.

The standard deviation of the tachogram in Figure 8 is 900 μs for the generator and 1.9 ms for the sensor. The correlation between the two signals is lower than 4 %; therefore, we can conclude that the jitter introduced by the sensor is in the order of $\sqrt{1.9^2 + 0.9^2}$ ms ≈ 2 ms.

The quantised data acquired by the overall system exhibits similar behaviour. It is slightly worse, presenting a jitter in the order of 2.3 ms; in any case, the jitter introduced by the sensor is close to the sample rate i.e. the lower bound for jitter performance.

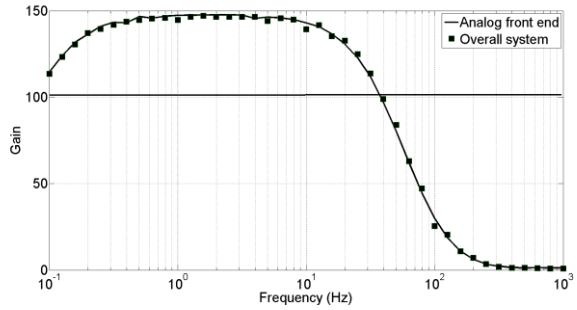

Figure 6. Bode plot of the gain relative to the SPR channels. Continuous line: analogue front end. Markers: overall acquisition system. The horizontal line represents the -3 dB cut off.

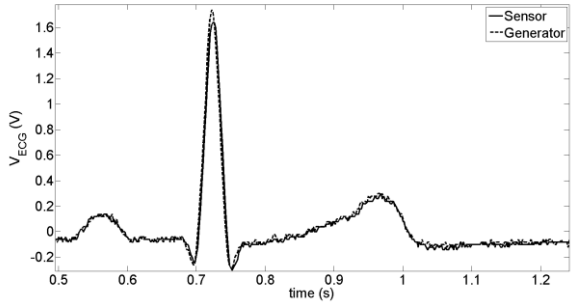

Figure 7. PQRST wave acquired at the generator (dashed line) and at the output of the analogue front end (solid line). It is possible to see a small jitter introduced by the analogue bandwidth.

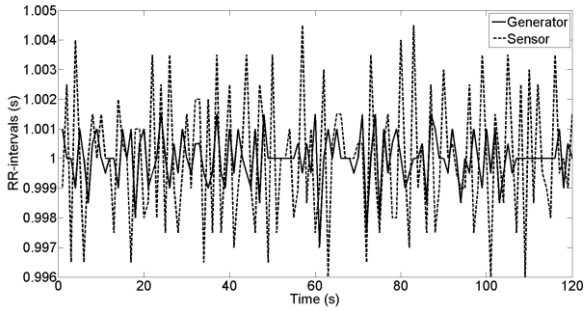

Figure 8. RR-intervals acquired from the sensor (dashed line) and from the generator (solid line).

3.3. Signal acquisition from hands in motion

Figure 9(a) shows a comparison between SPR_1 and SPR_2 when the hands are moving in the time interval of 2 mins. In particular, the rectangles evidence a small movement of the right hand and a strong movement of the left hand, with high disturbance of electrode contact. In the case of the small movement, the hand was just grasping an object; in the case of the strong movement, the person was tightening their fist against the electrode. In Figure 9(a), it is shown that without the movement, both channels are identical (trace in the interval 0 – 60 s), and when tightening the fist (trace in the interval 80 – 95 s), the artefact can be up to five times the actual SPR signal. With a single-channel EDA sensor, these peaks could be identified as stress peaks instead of motion artefacts. With a dual SPR channel, instead, it is quite simple, with several algorithms (e.g. independent component analysis, principal component analysis, adaptive filtering) used to discriminate artefacts from sympathetic pulses. Using adaptive filtration techniques, for example, it is possible to improve the accuracy to 10 %.

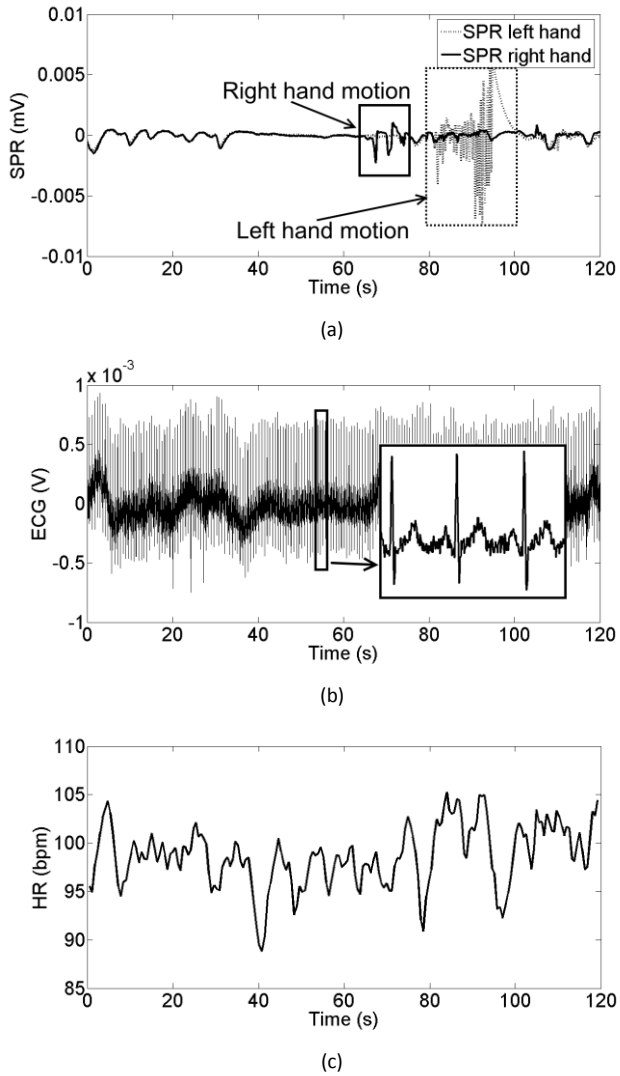

Figure 9. (a) Motion artefacts on the SPR channels; combining the two signals, it is possible to discriminate the sympathetic pulses; (b) ECG acquired from the hands; the box is a zoom of the ECG signal; (c) extracted heart rate.

Figure 9(b) shows the ECG, in the same session over the same time interval, acquired from the hands. Even if the trace is a little bit noisier with respect to traditional derivations on the chest, the PQRST wave is easily visible and processable. Figure 9(c) in fact, shows the extracted HR without any artefact due to noise or movements.

3.4. Comparison with chest acquisition

In previous subsections, we have characterised the performance of the sensor itself, neglecting the uncertainty due to the ECG-on-hands methodology. In this subsection, we compare the ECG readout from the proposed sensor on the hands, with a reference instrument acquiring ECG on the chest. In order to verify the performance of the proposed sensor, the ECG has been acquired simultaneously from the hands and from the chest, using the Shimmer system as a reference [23]. A Shimmer 3 EXG unit has been configured, with sample rate 1024 Sa/s posing three electrodes on the chest, at standard ECG positions V1 and V2, and the reference electrode was posed on the lower right side of the chest. The proposed sensor was connected as shown in Figure 1, and the acquisition ran simultaneously with the Shimmer system. The acquisition duration has been set to five minutes, which is typical for HRV analysis. During acquisition, no artefacts were recorded on both systems.

Figure 10(a) shows the ECG traces from the chest (red line) and from the hands (blue line). The ECG acquired from the hands is a little bit noisier (due to the acquisition being far from the heart), but the R-peaks are well identifiable on the trace. For this reason, it is inconvenient to implement other hardware/firmware filters on the sensor that could increase the jitter. Filtering instead in post processing, the noise can be easily removed without introducing jitter by filtering in forward and reverse directions.

Figure 10(b) shows the extracted tachograms from the chest (red line) and from the hands (blue line). From a qualitative point of view, it is plain to see that all the R-peaks have been identified without artefacts.

From a quantitative point of view, we compared the HRV analysis computed by Kubios from both systems. In Table 1, we show the obtained results. Table 1 compares several standard parameters for HRV analysis, like the mean RR interval, the standard deviation normal-to-normal (SDNN), the mean HR, and the root mean square of successive differences (RMSSD). As evidenced, even if the signal on the hands is noisier, the results differ less than 4 %. In addition, we evaluated the difference between the traces shown in Figure 10(b) and obtained a standard deviation on the difference of 4 ms. This result has the same order of magnitude of the sample rate; therefore, the ECG-

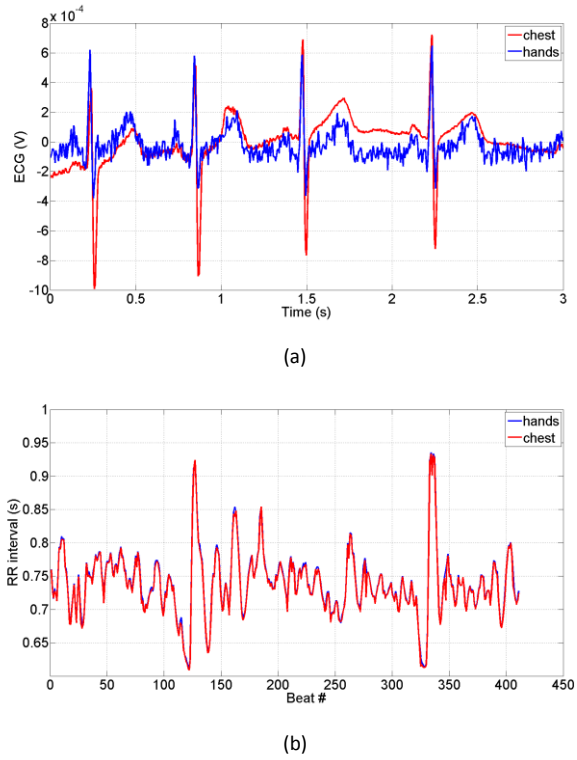

Figure 10. (a) Comparison between ECG acquired on the chest (red line) and on the hands (blue line); (b) RR tachogram extracted from the chest (red line) and from the hands (blue line).

Table 1. Comparison of HRV analysis performed from the proposed sensor and the Shimmer system.

	Proposed sensor	Shimmer	Δ%
Mean RR (ms)	739.85	736.58	0.44
SDNN (ms)	49.545	48.904	1.2
Mean HR (bpm)	81.453	81.808	-0.43
RMSSD (ms)	23.825	22.976	3.6

on-hands methodology can provide results with an accuracy comparable to the usual measurements on the chest.

4. CONCLUSION

The paper describes the design and characterisation of a wearable sensor for the simultaneous measurement of dual-channel EDA and ECG from the hands. Thanks to the dual-channel measurements, it is possible to improve the removal of motion artefacts that may affect EDA measurements.

The choice of ECG measurement from the hands improves the invasiveness of usual ECG sensors (which require the user to wear a vest or a chest band), and it is obtained using the same electrodes used for EDA.

The characterisation of the sensor showed high-level performance in terms of linearity, bandwidth, and jitter, even if the ECG is acquired where the signal-to-noise ratio is much lower than usual chest derivations.

REFERENCES

[1] D. S. Lee, T. W. Chung, B. G. Lee, Stress events detection of driver by wearable glove system, IEEE Sensors Journal 17, 1 (2017) pp. 194-204. 398 doi:10.1109/JSEN.2016.2625323

[2] N. Yoshimura, O. Koga, Y. Katsui, Y. Ogata, H. Kambara, Y. Koike. Decoding of emotional responses to user-unfriendly computer interfaces via electroencephalography signals, ACTA IMEKO 6 (2017) 2, pp. 93-98, DOI: https://dx.doi.org/10.21014/acta_imeko.v6i2.383.

[3] D. Tomoi, et al., Estimation of stress during car race with factor analysis, Proc. of the International Symposium on Micro-NanoMechatronics and Human Science (MHS), 23-25 November 2015, Nagoya, Japan, pp. 1-5, DOI: https://doi.org/10.1109/MHS.2015.7438258.

[4] E. Schmidt, R. Decke, R. Rasshofer, Correlation between subjective driver state measures and psychophysiological and vehicular data in simulated driving, Proc. of the IEEE Intelligent Vehicles Symposium (IV), 19-22 June 2016, Gothenburg, Sweden, pp. 1380-1385, DOI: https://doi.org/10.1109/IVS.2016.7535570.

[5] A. Affanni, Wearable instrument to measure simultaneously cardiac and electrodermal activities, Proc. of the IEEE International Symposium on Medical Measurements and Applications, MeMeA, 15-18 May 2016, Benevento, Italy, pp. 1-5.

[6] J. Ogorevc, G. Gersak, D. Novak, J. Drnovsek, Metrological evaluation of skin conductance measurements, Measurement 46, 9 (2013) pp. 2993–3001, DOI: https://doi.org/10.1016/j.measurement.2013.06.024.

[7] M. Schmidt, D. Penner, A. Burkl, R. Stojanovic, T. Schmann, P. Beckerle, Implementation and evaluation of a low-cost and compact electrodermal activity measurement system, Measurement 92 (2016) pp. 96-102, DOI: https://doi.org/10.1016/j.measurement.2016.06.007.

[8] A. Affanni, G. Chiorboli, D. Minen, Motion artifact removal in stress sensors used in "driver in motion" simulators, Proc. of the IEEE International Symposium on Medical Measurements and Applications (MeMeA), 15-18 May 2016, Benevento, Italy, pp. 1-6.

[9] A. Affanni, G. Chiorboli, Wearable instrument for skin potential response analysis in aal applications, Proc. of the 20th IMEKO TC4 Symposium on Measurements of Electrical Quantities: Research on Electrical and Electronic Measurement for the Economic Upturn, together with 18th TC4 International Workshop on ADC and DCA Modeling and Testing, IWADC, 15-17 September 2014, Benevento, Italy, pp. 807-811.

[10] A. Affanni, G. Chiorboli, Design and characterization of a real-time, wearable, endosomatic electrodermal system, Measurement 75 (2015), pp. 111-121.

[11] D. Bari, H. Aldosky, C. Tronstad, H. Kalvøy, Ø. Martinsen, Electrodermal responses to discrete stimuli measured by skin conductance, skin potential, and skin susceptance, Skin Research and Technology, issn:1600-0846, DOI: https://doi.org/465 10.1111/srt.12397.

[12] R. R. Fletcher, K. Amemori, M. Goodwin, A. M. Graybiel, Wearable wireless sensor platform for studying autonomic activity and social behavior in non-human primates, Proc. of the 34th Annual International Conference of the IEEE EMBS, 28 Aug. - 1 Sept., 2012, San Diego, California, USA, pp. 4046-4049.

[13] F. Seoane, I. Mohino-Herranz, J. Ferreira, L. Alvarez, R. Buendia, D. Ayllón, C. Llerena, R. Gil-Pita, Wearable biomedical measurement systems for assessment of mental stress of combatants in real time, Sensors 14, 4 (2014) pp. 7120-7141.

[14] F. Seoane, I. Mohino-Herranz, J. Ferreira, L. Alvarez, R. Buendia, D. Ayllón, C. Llerena, R. Gil-Pita, Sensorized garments and textrode-enabled measurement instrumentation for ambulatory assessment of the autonomic nervous system response in the ATREC project, Sensors 13, 7 (2013) pp. 8977-9015.

[15] A. Porta, E. Tobaldini, S. Guzzetti, R. Furlan, N. Montano, T. Gnecchi-Ruscone, Assessment of cardiac autonomic modulation during graded head-up tilt by symbolic analysis of heart rate variability, Am J Physiol Heart Circ Physiol 293, 1 (2007) pp. 702-708.

[16] T. Ziemssen, M. Reimann, J. Gasch, H. Rudiger, Trigonometric regressive spectral analysis: an innovative tool for evaluating the

autonomic nervous system, J Neural Transm 120, 1 (2013) pp. 27-33.
[17] H. Rudiger, L. Klinghammer, K. Scheuch, The trigonometric regressive spectral analysis-a method for mapping of beat-to-beat recorded cardiovascular parameters on to frequency domain in comparison with Fourier transformation, Computer Methods and Programs in Biomedicine 58 (1999) pp. 1-15.
[18] A. L. Smith, H. Owen, K. J. Reynolds, Heart rate variability indices for very short-term (30 beat) analysis. Part 1: survey and toolbox, J Clin Monit Comput 27 (2013) pp. 569-576.
[19] A. L. Smith, H. Owen, K. J. Reynolds, Heart rate variability indices for very short-term (30 beat) analysis. Part 2: validation, J Clin Monit Comput 27 (2013) pp. 577-585.
[20] RIGOL Technologies Inc., MSO2000A/DS2000A Series Digital Oscilloscope user's guide, August 2015, http://int.rigol.com/File/TechDoc/20160830/MSO2000A&DS2000A_UserGuide_EN.pdf
[21] Kubios, Kubios HRV software http://kubios-hrv.software.informer.com/
[22] W. Boucsein, Electrodermal Activity, Springer, New York Dordrecht Heidelberg London, 2012, ISBN 978-1-4614-1126-0 https://www.springer.com/us/book/9781461411253
[23] Shimmer Realtime technologies Ltd, Shimmer User Manual, 2017, https://www.shimmersensing.com/